

Single-crystalline monolayer semiconductors with coherent quantum transport by vicinal van der Waals epitaxy

Received: 25 October 2024

Accepted: 8 October 2025

Published online: 27 November 2025

 Check for updates

Gunho Moon^{1,2,8}, Suk-Ho Lee^{1,2,8}, Hyunje Cho^{1,2,8}, Heewon Park^{1,2}, Heonsu Ahn^{1,2}, Chang-Won Choi^{1,2}, Sera Yang^{1,2}, Seung-Hyun Shin³, Jinjae Kim⁴, Jong Yun Choi^{1,2}, Seok Young Min^{1,2}, Sumin Lee^{1,2}, Hyunjin Jung^{3,5}, Jaeyoung Kim⁵, Jewook Park¹, Han Woong Yeom^{3,5}, Gil-Ho Lee³, Myungchul Oh^{1,6}, Jong-Hoon Kang^{1,2}, Hyunyoung Choi^{1,4}, Cheol-Joo Kim^{1,7}, Jonghwan Kim^{1,2,3}, Si-Young Choi^{1,2} & Moon-Ho Jo^{1,2,3} ✉

Monolayers of transition metal dichalcogenides, such as molybdenum disulfide, are a potential platform for two-dimensional carrier transport. However, although single-crystalline monolayer channels have been grown at the wafer scale using unidirectional coalescence epitaxy, achieving coherent two-dimensional transport at similar scales remains challenging. This is mainly due to the presence of residual crystalline defects, such as one-dimensional extended and point defects, which emerge when multiple grains coalesce. Here we report an epitaxial growth of single-crystal molybdenum disulfide monolayers at wafer scales in which these defects are minimized by coalescence kinetics control on vicinal sapphire substrates. The resulting channels exhibit coherent transport—manifesting as weak localization and the onset of quantum Hall effects at low temperature—as well as a Hall mobility of $1,200 \text{ cm}^2 \text{ V}^{-1} \text{ s}^{-1}$. These coherent channels are used to create arrays of field-effect transistors, which exhibit an average mobility of around $100 \text{ cm}^2 \text{ V}^{-1} \text{ s}^{-1}$ and a minimum subthreshold swing of around 65 mV dec^{-1} at room temperature.

Precise control over lattice defects in monolayer (ML) crystals of transition metal dichalcogenides is essential to achieve intrinsic two-dimensional (2D) carrier transport that is free of carrier scattering and phase decoherence^{1–4}. A prominent strategy for the wafer-scale production of single-crystalline transition metal dichalcogenide MLs is epitaxial growth on vicinal substrates (that is, substrates that have been cut slightly off one of their main crystallographic axis, resulting in a series of atomically high steps)^{5–12}.

These commonly use the unidirectional coalescence growth of multiple grains, where the local nucleation and ensuing unidirectional grain growth are registered on the vicinal steps and terraces, facilitating single-crystalline textures that are free of grain boundaries (Supplementary Table 1 provides a comparison of the reported growth schemes and properties).

Nonetheless, local defects inevitably persist when multiple grains coalesce due to growth kinetics instabilities and atomic

¹Center for van der Waals Quantum Solids, Institute for Basic Science (IBS), Pohang, Korea. ²Department of Materials Science and Engineering, Pohang University of Science and Technology (POSTECH), Pohang, Korea. ³Department of Physics, Pohang University of Science and Technology (POSTECH), Pohang, Korea. ⁴Department of Physics and Astronomy, Seoul National University, Seoul, Korea. ⁵Center for Artificial Low Dimensional Electronic Systems, Institute for Basic Science (IBS), Pohang, Korea. ⁶Department of Semiconductor Engineering, Pohang University of Science and Technology (POSTECH), Pohang, Korea. ⁷Department of Chemical Engineering, Pohang University of Science and Technology (POSTECH), Pohang, Korea. ⁸These authors contributed equally: Gunho Moon, Suk-Ho Lee, Hyunje Cho. ✉ e-mail: mhjo@postech.ac.kr

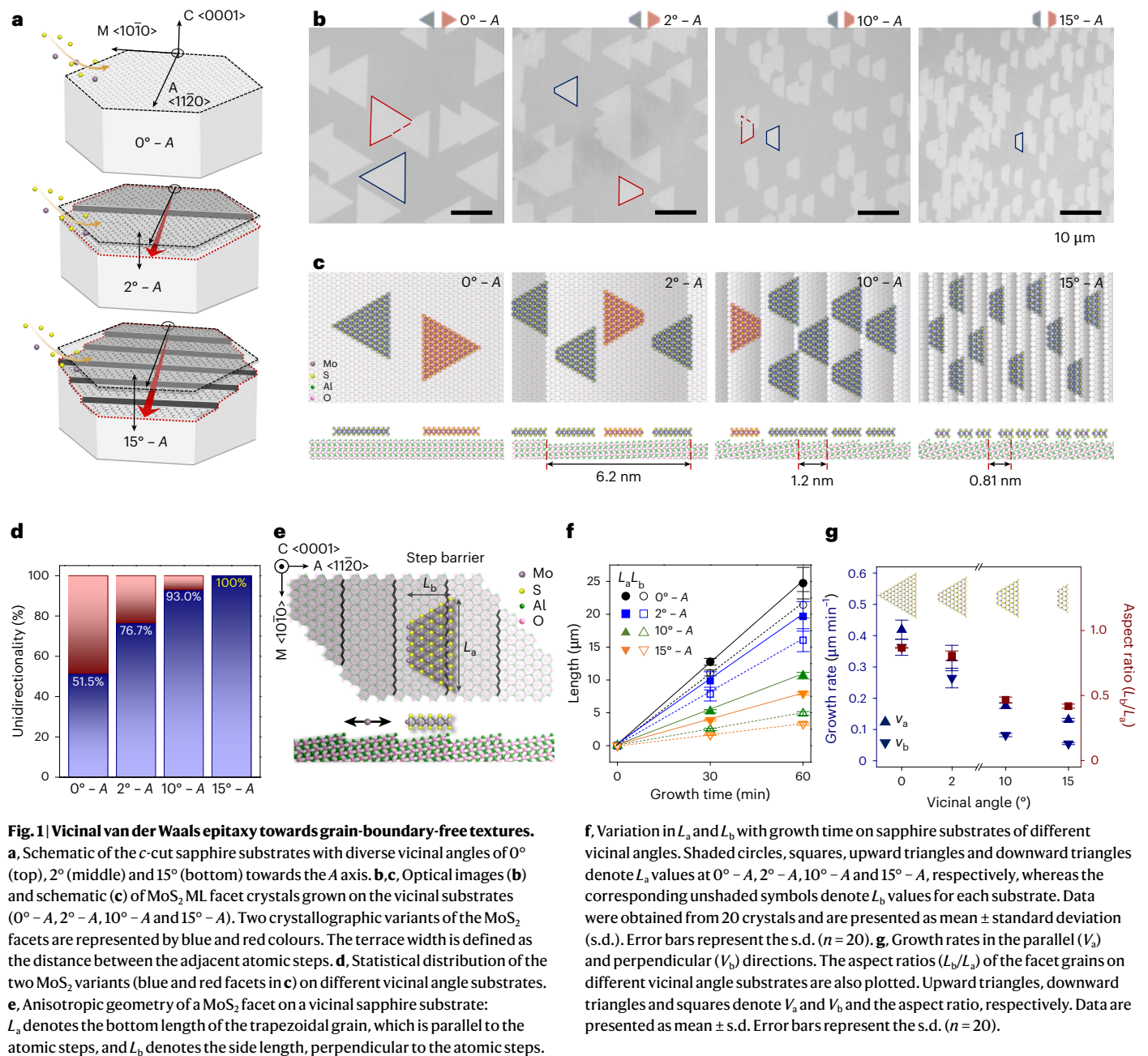


Fig. 1 | Vicinal van der Waals epitaxy towards grain-boundary-free textures. **a**, Schematic of the *c*-cut sapphire substrates with diverse vicinal angles of 0° (top), 2° (middle) and 15° (bottom) towards the *A* axis. **b, c**, Optical images (**b**) and schematic (**c**) of MoS₂ ML facet crystals grown on the vicinal substrates (0° - *A*, 2° - *A*, 10° - *A* and 15° - *A*). Two crystallographic variants of the MoS₂ facets are represented by blue and red colours. The terrace width is defined as the distance between the adjacent atomic steps. **d**, Statistical distribution of the two MoS₂ variants (blue and red facets in **c**) on different vicinal angle substrates. **e**, Anisotropic geometry of a MoS₂ facet on a vicinal sapphire substrate: L_a denotes the bottom length of the trapezoidal grain, which is parallel to the atomic steps, and L_b denotes the side length, perpendicular to the atomic steps.

f, Variation in L_a and L_b with growth time on sapphire substrates of different vicinal angles. Shaded circles, squares, upward triangles and downward triangles denote L_a values at 0° - *A*, 2° - *A*, 10° - *A* and 15° - *A*, respectively, whereas the corresponding unshaded symbols denote L_b values for each substrate. Data were obtained from 20 crystals and are presented as mean ± standard deviation (s.d.). Error bars represent the s.d. ($n = 20$). **g**, Growth rates in the parallel (V_a) and perpendicular (V_b) directions. The aspect ratios (L_b/L_a) of the facet grains on different vicinal angle substrates are also plotted. Upward triangles, downward triangles and squares denote V_a and V_b and the aspect ratio, respectively. Data are presented as mean ± s.d. Error bars represent the s.d. ($n = 20$).

stoichiometry^{4,13,14}, which then obscure coherent 2D transport. It is, therefore, critical to address these local defects during growth and to recognize their impacts on the carrier transport characteristics^{15–17}. In this Article, we identify the local dislocation cores associated with one-dimensional extended and zero-dimensional point defects in such single-crystalline textures, which can cause shallow-angle (<1–2°) misalignments for the case of ML molybdenum disulfide (MoS₂) grown on two-inch sapphire wafers. We then develop a growth scheme in which the dislocation cores and point defects are eliminated by the careful kinetic control of coalescence epitaxy. Low-temperature transport in the resulting MoS₂ films shows coherent 2D carrier transport, as manifested by weak localization and the onset of quantum Hall effects, along with a high Hall mobility of 1,200 cm² V⁻¹ s⁻¹. We use the films as the channel material in field-effect transistor (FET) arrays and show that the resulting devices exhibit an average room-temperature mobility of ~100 cm² V⁻¹ s⁻¹ and subthreshold swing (SS) of 65–75 mV dec⁻¹.

Vicinal van der Waals epitaxy towards grain-boundary-free textures

We used *c*-plane sapphire substrates, cut with varying vicinal angles towards the *A* axis of 0°, 2°, 10° and 15° (Fig. 1a–c and Supplementary Figs. 1 and 2) for the vicinal epitaxy at a growth temperature (T_g) of 810–850 °C. MoS₂ MLs possess three-fold in-plane rotation symmetry, and their epitaxial stacking on the planar *c*-plane sapphires results in two crystallographic variants with an equivalent formation energy^{6,7}. Such variants are 60° rotated from one another, as indicated by the blue and red triangles in Fig. 1b, forming mirror-twin boundaries. In other words, they naturally crystallize bicrystals on the planar *c*-plane sapphires^{18,19}. It is at the atomic steps at which unidirectional nucleation is initiated, as reported for various transition metal dichalcogenide single-crystal MLs^{5–12}. However, for unidirectional coalescence growth, the role of such step edges on vicinal substrates is yet to be fully understood. Epitaxial growth on substrates with varying vicinal angles—and thus the step and terrace density

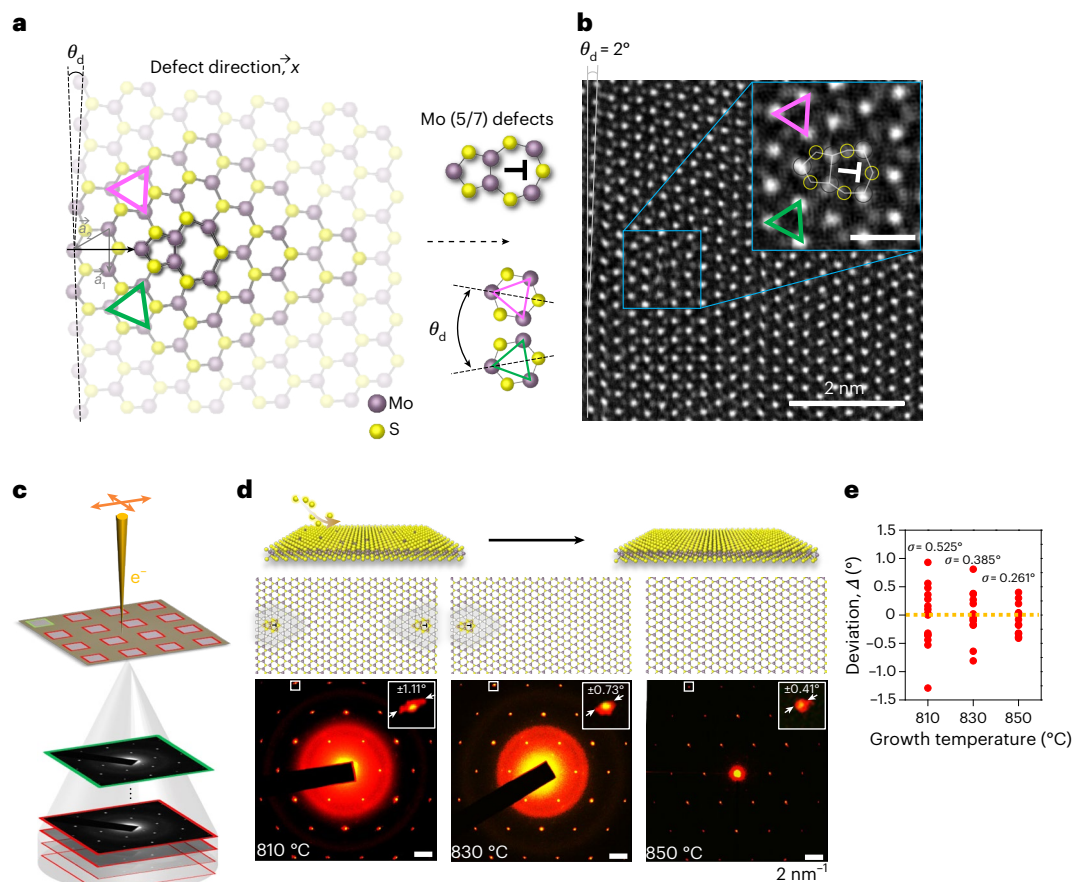


Fig. 2 | Dislocation cores and point-defects-free crystalline textures.

a,b, Schematics (**a**) and HAADF-STEM images (**b**) of a local dislocation core near a Mo (5/7) point defect. The misfit angle (θ_d) represents the deviation between two adjoining grains, depicted as pink and green triangles. **c**, Acquisition of the collection of SAED patterns in the 16 growth patterns. **d**, Overlaid SAED patterns

from epitaxial MoS₂ single-crystal MLs grown at different T_G values, with the magnified fifth-order (030) peaks shown in the insets. Schematics (top) illustrate the elimination of local deformation and point defects at different T_G values. **e**, Angle deviations of the (030) peaks from the epitaxial single-crystal MoS₂ MLs grown at different T_G values, showing the cleanest crystallinity at $T_G = 850$ °C.

systematically vary—enables us to take a closer look at the progression of nucleation and growth (Fig. 1b,c). For example, nucleation occurs predominantly on the terrace, when the terrace width (the distance between the adjacent steps) of the 2° vicinal substrate is ~6 nm. It is, however, much shorter than 1 nm for the 15° vicinal substrate, where nucleation is solely on the atomic steps (Supplementary Fig. 2). Here we maintained a slow lateral growth rate of $<0.5 \mu\text{m min}^{-1}$ by controlling the flow rate of metal–organic sources under lower partial pressures ($p(\text{Mo}(\text{CO})_6) \approx 10^{-6}$ torr and $p(\text{C}_2\text{H}_5)_2\text{S} \approx 10^{-3}$ torr) in the near-equilibrium growth regime^{20–22}. We observed systematic variation in the size and shape of the individual crystal facet on substrates with different vicinal angles, as summarized below. First, the facet size and shape gradually change from a larger triangle to a smaller trapezoid on the denser steps. Second, the total numbers of facets increase on the denser steps. Third, the facet in-plane orientation becomes unidirectional at higher vicinal angles, facilitating mirror-twin-boundary-free single-crystal textures, as statistically plotted in Fig. 1d (Supplementary Figs. 3–7 provide more details). This indicates that the vicinal steps, as the preferential nucleation sites, primarily promote unidirectional growth, consistent with previous studies^{6–11}. In addition, our observations directly verify the anisotropic growth variations in a quantitative manner. That is, by examining variation in the individual facet shapes, we measure the directional growth rate (V_a and V_b), in parallel (L_a) and perpendicular (L_b) to the step edges (Fig. 1e), where V_a is always greater than V_b at all vicinal angles and both V_a and V_b are greater at lower vicinal angles (Fig. 1f,g). This reveals that the vicinal step also acts as the diffusion barrier of the adatoms²³, particularly for perpendicular growth depicted in Fig. 1e

(Supplementary Figs. 8 and 9 show the analyses of the anisotropic growth profile on vicinal *c*-plane sapphire substrates).

Dislocation cores and point-defects-free crystalline textures

During unidirectional grain coalescence in the apparently single-crystalline textures, any deviation from the perfect orientational alignment of each grain can lead to local dislocation lines^{7,13,14}, often accompanied by the presence of point defects and/or their clusters along the subunit-cell translations. This is qualitatively different from usual grain boundaries with distinct tilt angles, extended over several micrometres in poly-crystalline MLs, and is hidden under electron microscopy. Figure 2a illustrates an example of such local deformation near a Mo pentagon–heptagon (5/7) point defect, known to be the most energetically favourable point defects with the smallest Burgers vector²⁴. The presence of a (5/7) point defect causes the two adjoining MoS₂ local grains, indicated by pink and green triangles, to deviate by a misfit angle (θ_d), along the defect direction vector \vec{x} . In our growth, this misfit angle can be as large as 1–2°, as verified by high-angle annular dark-field (HAADF) scanning transmission electron microscopy (STEM) images (Fig. 2b). These local defects can be formed for several reasons, such as in-plane strain, unwanted out-of-plane tilting and off-stoichiometry during the growth¹³. Then, we optimized the growth conditions by carefully tuning the T_G value and precursor flow rate. In general, the higher T_G value facilitates proper stoichiometry with reduced composition uncertainty and, thus, reduced off-stoichiometric defects^{25,26},

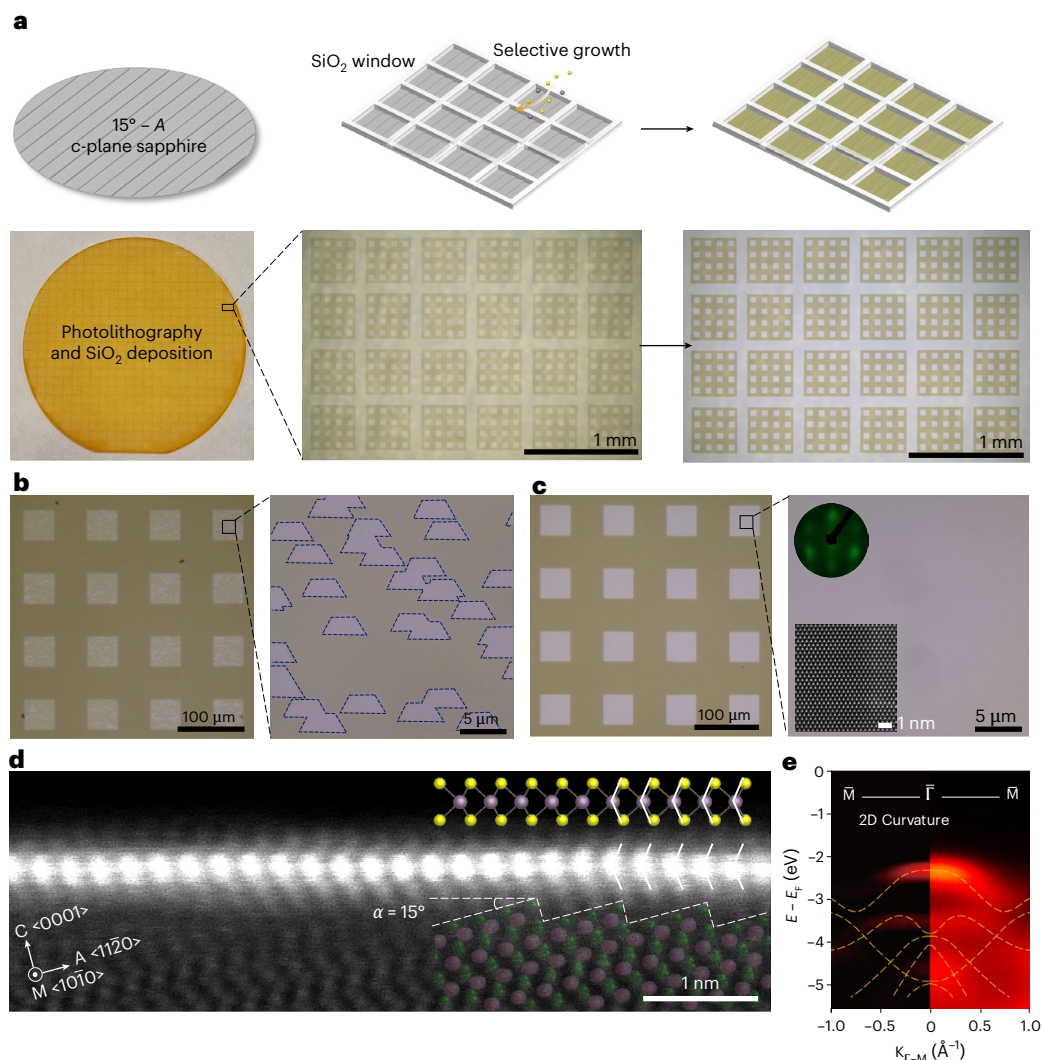


Fig. 3 | Pattern growth of single-crystal MoS₂ MLs in wafer scales and their electronic structures. **a**, Patterned growth of single-crystal MoS₂ MLs on a two-inch, 15° c-sapphire wafer. The patterns were lithographically defined with SiO₂ windows. Schematics (top) and optical images (bottom) of the samples before and after the selective growth. **b,c**, Optical images of single-crystal MoS₂ MLs grown on the SiO₂ patterns in the early growth stage (**b**) and after growth (**c**).

Top inset: a representative LEED pattern; bottom inset: an in-plane HAADF-STEM image. **d**, Cross-sectional HAADF-STEM image and the corresponding atomic structure of an epitaxial MoS₂ ML on a 15° sapphire substrate. **e**, ARPES band map and 2D curvature of the epitaxial single-crystal MoS₂ MLs along the $\Gamma - \bar{M}$ high-symmetry direction, with the density-functional-theory-based band calculations³⁰ plotted as the orange dotted lines.

as well as allows adatoms to migrate over longer distances to energetically favourable sites to release the residual stress at the grain boundaries^{27,28}. The degree of this local deformation on the ML crystals was assessed by selective-area electron diffraction (SAED) patterns from 16 box regions of $50 \times 50 \mu\text{m}^2$, which are 100 μm apart within a single-crystal film, grown at T_G values of 810 °C, 830 °C and 850 °C (Supplementary Fig. 10 provides more details). As shown in Fig. 2c,d, we overlaid the 16 SAED patterns from each sample to examine the misfit dispersion by closely analysing the fifth-order peak (030). In Fig. 2d (insets, bottom), we observed that the width of the streaky (030) patterns is progressively larger at lower T_G . Figure 2e shows the statistical distribution of the misfits, calculated by measuring the angles between each peak (indicated by red dots) and the median peak (indicated by the yellow line). For $T_G = 850$ °C, we found the minimum misfit distribution down to $\pm 0.41^\circ$, which can be regarded as the optimum single crystal, free from both dislocations and point defects, for our low-temperature transport investigations. We also verified a low sulfur-vacancy density of $3 - 6 \times 10^{12} \text{cm}^{-2}$ in our epitaxial MoS₂ single crystals by scanning tunnelling microscopy (STM) and HAADF-STEM images (Supplementary Figs. 11 and 12, respectively).

Crystal and electronic structures of MoS₂ single-crystalline MLs in wafer scales

Having optimized the growth conditions for the cleanest MoS₂ ML single crystals at $T_G = 850$ °C, we fabricated the selectively patterned MoS₂ ML channels ($50 \times 50 \mu\text{m}^2$) into square SiO₂ windows on two-inch-wafer c-sapphire substrates with a vicinal angle of 15°. Figure 3a shows the schematics of the selective growth (Supplementary Figs. 13 and 14 show a comparison of the growth behaviour with/without SiO₂ masks)²⁹, where we patterned square SiO₂ trenches to define the growth areas of c-sapphire substrates, as well as the corresponding optical images (Methods). We verified that, within the growth panels, the trapezoidal MoS₂ ML grains gradually coalesce and seamlessly stitch into the single-crystalline films (Fig. 3b,c and Supplementary Fig. 15). The in-plane crystal orientation in each pattern was confirmed by second-harmonic generation (SHG) measurements (Supplementary Figs. 16 and 17). The low-energy electron diffraction (LEED) pattern, obtained using a submillimetre-sized electron beam from the synchrotron source at beamline 4A2 of the Pohang Light Source, reveals three bright spots that indicate C₃ symmetry (Fig. 3c, inset (right)), and it is consistent over the different spots, which are

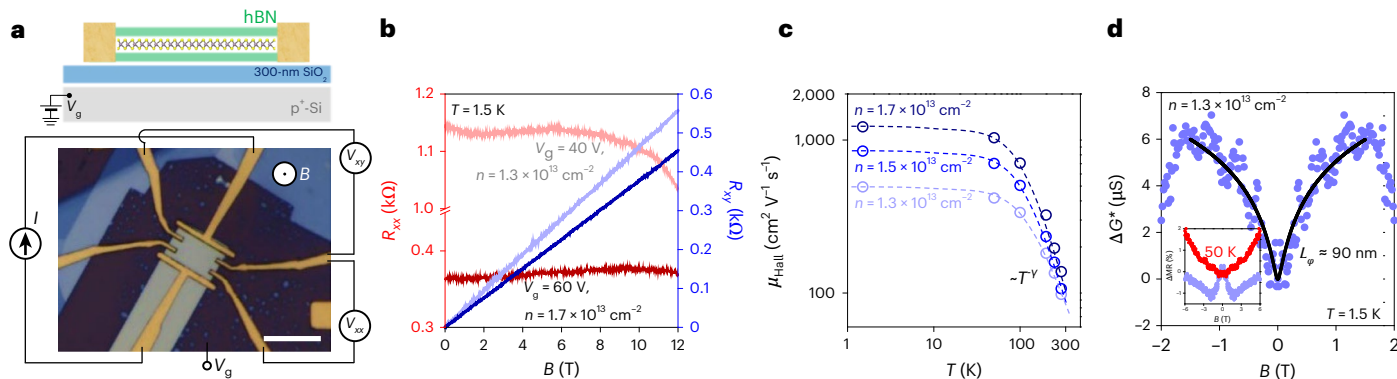


Fig. 4 | Coherent transport in epitaxial single-crystal MoS₂ ML films.

a, Schematics and optical image of the Hall-bar device, where the single-crystal MoS₂ ML channel is encapsulated between the top and bottom hBN layers. Scale bar, 10 μm. **b**, R_{xx} (red curves) and R_{xy} (blue curves) of the Hall device as a function of the magnetic field at different gate voltages (V_g), measured at 1.5 K. The light-coloured curves represent $V_g = 40$ V, and the deep-coloured curves correspond to $V_g = 60$ V. **c**, μ_{Hall} as a function of temperature for different n values. For $T > 100$ K, μ_{Hall} follows a power-law relationship with temperature, where

$\mu_{\text{Hall}} \approx T^{-\gamma}$, with the exponent γ ranging from 1.5 to 2.1. **d**, Magnetoconductance $\Delta G^*(B)$, defined as $\Delta G^*(B) = [G_{xx}(+B) + G_{xx}(-B)]/2 - G_{xx}(B=0 \text{ T})$, measured at $n = 1.3 \times 10^{13} \text{ cm}^{-2}$ and $T = 1.5$ K, where G_{xx} is the longitudinal conductance. The solid black line is a fit using the HLN model within the range of -1.5 T and 1.5 T. Inset: $\Delta \text{MR} = [R_{xx}(B) - R_{xx}(B=0 \text{ T})]/R_{xx}(B=0 \text{ T}) \times 100\%$ for 1.5 K (purple) and 50 K (red), where $R_{xx}(B)$ is the symmetrized longitudinal resistance, given by $R_{xx}(B) = [R_{xx}(+B) + R_{xx}(-B)]/2$.

1 mm apart from each other across the entire sample (Supplementary Fig. 18). The epitaxial relation to the c-plane sapphire was examined by cross-sectional STEM (Fig. 3d), showing that the MoS₂ MLs are epitaxially aligned along the $\langle 10\bar{1}0 \rangle$ orientation of the 15° vicinal sapphire. The electronic structures of our epitaxial MoS₂ single-crystal MLs were directly measured with angle-resolved photoemission spectroscopy (ARPES) with a synchrotron X-ray radiation ($h\nu = 60$ eV) beam size of ~ 50 μm (Fig. 3e and Methods), where we clearly found the band dispersions along the $\bar{\Gamma} - \bar{M}$ high-symmetry directions of the Brillouin zone (data for the $\bar{\Gamma} - \bar{K}$ direction are shown in Supplementary Fig. 19a). Note that the left half-panel shows its second derivative. The absence of split bands at $\bar{\Gamma}$ indicates ML homogeneity without unwanted bilayer overgrowth³⁰. Distinct single-band dispersion without mixing for each $\bar{\Gamma} - \bar{M}$ and $\bar{\Gamma} - \bar{K}$ direction illustrates the uniform orientation of multiple grains, confirming the exact single-crystal texture³¹. This is also consistent with the Fermi map at $E - E_F = -3.9$ eV (Supplementary Fig. 19b). In particular, the 2D curvature plot of the upper valence band is consistent with the computed bands³², with the minimal energy compression indicating fewer defects, doping and stress³⁰.

Coherent transport in epitaxial MoS₂ single-crystal ML films

Our MoS₂ single-crystalline ML channels (the growth patterns are shown in Fig. 3) were configured to a $5 \times 10 \text{ μm}^2$ Hall bar to be measured for carrier transport under an out-of-plane magnetic field (B) at low temperatures. Figure 4a shows a schematic and optical image of the Hall bar, where the MoS₂ ML is encapsulated between the top and bottom hexagonal boron nitride (hBN) layers with Ti/Au edge contacts^{1,33}. Figure 4b shows the perpendicular (R_{xy}) and longitudinal (R_{xx}) resistances at 1.5 K, leading to a high Hall mobility (μ_{Hall}) of $\sim 1,200 \text{ cm}^2 \text{ V}^{-1} \text{ s}^{-1}$, when the carrier density (n) was induced to be $1.7 \times 10^{13} \text{ cm}^{-2}$ at $V_g = 60$ V in the n-type regime (Supplementary Fig. 20 shows the result at a different carrier density and Supplementary Fig. 21 shows a larger-sized Hall-bar measurement). This μ_{Hall} value is comparable with that of a single-crystal flake of chemical-vapour-deposition-grown MoS₂ ML ($\sim 1,400 \text{ cm}^2 \text{ V}^{-1} \text{ s}^{-1}$; ref. 1) and to the theoretical calculation³⁴ of $\sim 1,500 \text{ cm}^2 \text{ V}^{-1} \text{ s}^{-1}$ at the reduced charged impurity density of $5 \times 10^{11} \text{ cm}^{-2}$. In comparison, a low-temperature Hall mobility of $\sim 5,000 \text{ cm}^2 \text{ V}^{-1} \text{ s}^{-1}$ has been achieved on exfoliated flakes³. In Fig. 4b, the R_{xx} value at $V_g = 40$ V begins to decline from the constant value at $B > 10$ T, diverging from the classical Hall effect, which can be attributed to the onset of Shubnikov–de Haas oscillations; when μ_{Hall} is $\sim 1,000 \text{ cm}^2 \text{ V}^{-1} \text{ s}^{-1}$, we estimate the onset of

the Shubnikov–de Haas oscillation, $B_{\text{onset}} > \mu^{-1}$ (ref. 35), to begin at ~ 10 T. The μ_{Hall} versus T curve is given in Fig. 4c, where we observe that μ_{Hall} monotonously increases with decreasing T and eventually saturates to a constant value at low temperatures. At $T > 100$ K, the carrier transport is primarily dominated by optical phonon scattering³⁶, as described by a power law ($\mu_{\text{Hall}} \approx T^{-\gamma}$), where γ varies from 1.5 to 2.1. At low temperatures, where phonon scattering becomes negligible with a constant μ_{Hall} value, the carrier transport is governed by either long-range Coulomb scattering or short-range scattering caused by lattice defects. The unintentional Coulomb potential from interfacial charge impurities can be effectively screened by charge carriers in the channels; thus, an increase in the charge carrier density, n , leads to enhanced mobility^{37,38}. However, short-range scattering results in a μ_{Hall} value that is less sensitive to n (refs. 39,40). In our case (Fig. 4c), the pronounced increase in the saturated μ_{Hall} values with n , which we tuned by the applied gate voltage, suggests that the short-range scattering from point defects and disorders is minimized in our optimum-growth single crystals. In fact, we found the overall degradation of μ in the entire T range when the growth was performed at 810 °C (Supplementary Fig. 22), thereby allowing a larger fraction of dislocation cores and point defects (Fig. 2).

The magnetoresistance (MR) at 1.5 K in our Hall bar does not follow a simple quadratic B dependence. Instead, it displays a noticeable cusp at $B = 0$ T (Fig. 4d). This negative low-field MR correction is a signature of weak localization, where the quantum interference effectively increases the channel resistivity near $B = 0$ T. Within the Hikami–Larkin–Nagaoka (HLN) model for 2D weak localization⁴¹, we extracted the phase coherence length (L_ϕ) in our Hall device (Methods) to be around 90 nm for $n = 1.3 \times 10^{13} \text{ cm}^{-2}$ at 1.5 K. This is again comparable with those measured in exfoliated MoS₂ single crystals under similar conditions^{42–44}, ensuring the quantum-grade crystal quality of our MoS₂ MLs, free from scattering defects. This low-field MR feature disappears at higher temperatures, where the phase coherence is lost in the classical diffusive regime (Fig. 4d, inset).

Performance of epitaxial MoS₂ ML FET arrays

We integrated our MoS₂ ML channel patterns into FET arrays, by transferring onto HfO₂ (10 nm)/p⁺-Si substrates (Fig. 5a). Note that the FET channels are not hBN passivated for practical applications. We achieved ohmic contacts with bismuth as the source/drain contacts⁴⁵, as verified by the I – V characteristics (Fig. 5b). Figure 5c shows the transfer characteristics (I – V_g) of an FET, where the channel length and width are ~ 2.2 μm and 5.0 μm, respectively, demonstrating the sharpest SS

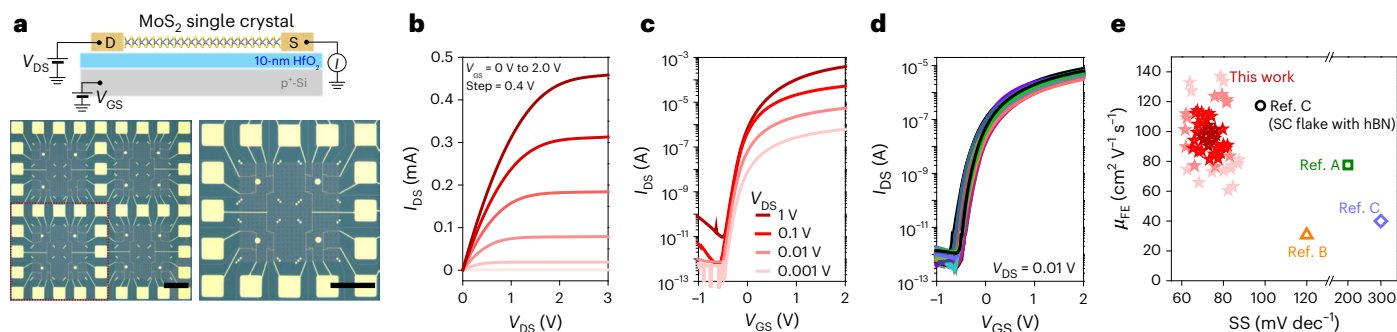


Fig. 5 | High performance of epitaxial MoS₂ ML FET arrays. **a**, Schematics and optical images of the FET arrays on single-crystal MoS₂ MLs patterns, transferred onto a HfO₂ (10 nm)/p⁺-Si substrate. The bottom-left optical image shows the full array, whereas the right image shows a close-up view of 16 FETs within the array. Scale bars, 100 μ m. **b**, **c**, Output (**b**) and transfer (**c**) characteristics of a

representative FET, measured at room temperature. **d**, Transfer characteristics of all 64 FETs measured at $V_{DS} = 0.01$ V. **e**, Benchmark plot, comparing μ_{FE} and SS of the FET arrays of this work (red stars) with FETs using epitaxially coalesced single-crystalline (SC) MoS₂ MLs from earlier works (indicated as Ref. A, Ref. B and Ref. C, adapted from refs. 6,8,11, respectively).

of 65 mV dec⁻¹ at room temperature and on/off current ratio exceeding $\sim 10^7$. We plot the statistical distribution of the FET mobility (μ_{FE}) and the SS, measured on 64 FETs within the array (Fig. 5d,e), where we attained an average μ_{FET} of ~ 100 cm² V⁻¹ s⁻¹, with an SS of 65–75 mV dec⁻¹ (Supplementary Fig. 23). We highlight the FET performance metrics, with the SS being close to the theoretical limit of ~ 60 mV dec⁻¹, and μ_{FET} being superior to those of the recent demonstrations on wafer-scale epitaxial MoS₂ MLs^{6,8,10,11}. For example, earlier examples of epitaxial MoS₂ ML single crystals on *c*-plane sapphire made by similar coalescence growth schemes demonstrated FET arrays with an average μ_{FET} of 78 cm² V⁻¹ s⁻¹ and SS of ~ 120 mV dec⁻¹. The near-ideal SS value is also related to the substantial reduction in defect density within our single-crystal MoS₂ MLs, in that the charge trap process at the defects can cause a less-steep SS^{46–49}.

Conclusions

We have reported an optimized growth technique for MoS₂ on vicinal substrates that can reduce kinetic instabilities and off-stoichiometry defects. In particular, by controlling the coalescence kinetics of multiple unidirectional grains, we were able to create wafer-scale, single-crystalline MoS₂ MLs with coherent quantum transport. Investigations of large-scale Hall-bar geometries at low temperatures showed a Hall mobility of 1,200 cm² V⁻¹ s⁻¹ and a signature of weak localization. When the coherent layers were integrated into arrays of FETs, the resulting devices exhibited an average room-temperature mobility of ~ 100 cm² V⁻¹ s⁻¹ and minimum SS of ~ 65 mV dec⁻¹. Our work provides an approach to grow quantum transport platforms at wafer scales, offering a new avenue to develop 2D quantum electronics at the circuit level, as well as advanced 2D semiconductor technology.

Methods

Epitaxial growth of MoS₂ ML crystals on *c*-plane sapphire substrates of varying vicinal angles

MoS₂ ML crystals were epitaxially grown on *c*-plane sapphire substrates with varying vicinal angles (0°, 2°, 10° and 15°) relative to the *A* axis, using a custom-built metal–organic chemical vapour deposition system. The substrates were placed in a hot-walled 2.6-inch quartz tube, and the furnace was ramped up to $T_G = 850$ °C for 20 min. The total pressure was maintained at 1.3 torr under a carrier gas flow of 80 s.c.c.m. for Ar (99.9999%) and 4 s.c.c.m. for H₂ (99.9999%). During the growth process, Mo(CO)₆ and (C₂H₅)₂S precursors were supplied by individual mass flow controllers. The flow rates of the precursors were optimized at 0.3 s.c.c.m. for Mo(CO)₆ and 0.6 s.c.c.m. for (C₂H₅)₂S. Note that both precursors were kept in bubbler-type canisters at a constant pressure of 400 torr with Ar at room temperature. The growth of MoS₂ ML films on the various vicinal sapphire substrates was conducted for 40–90 min.

The growth time of MoS₂ ML films on a vicinal 15° substrate was the longest (90 min) due to atomic steps acting as diffusion barriers, whereas it reduces to 40 min for growth on 0° substrates.

Fabrication of SiO₂ windows on *c*-plane sapphire substrates for pattern growth

For the fabrication of SiO₂ windows on two-inch sapphire wafers, conventional photolithography was used. A lift-off resist was initially spin coated onto the sapphire wafers to facilitate the lift-off process, followed by a layer of positive photoresist (AZ MIR 701), which was patterned using a contact aligner (MA/BA8 Gen4). A 20-nm layer of SiO₂ was then deposited onto the photoresist-coated sapphire wafers via electron-beam evaporation. The lift-off process was carried out by soaking the wafers in acetone for 1.5 h with sonication. Afterwards, the wafers were rinsed in isopropanol with sonication for 5 min, soaked in AZ 300 MIF developer for 2 min to eliminate the lift-off resist layer and finally rinsed in deionized water for 2 min.

Transmission electron microscopy analysis

For in-plane transmission electron microscopy (TEM) observations, MoS₂ ML SCs were transferred onto Cu TEM grids (holey carbon film grids for dark-field TEM imaging and QUANTIFOIL grids for STEM analysis) using a polymethyl methacrylate (PMMA)-assisted wet-transfer technique. Cross-sectional TEM specimens were prepared using a focused ion beam (Helios NanoLab G3 CX, FEI). To protect the specimens, a 20-nm-thick amorphous carbon layer was deposited using a carbon coater. STEM images and SAED patterns (Figs. 2b,d and 3c,d and Supplementary Figs. 10, 12 and 15) were obtained using a JEOL JEM-ARM 200F device with a Cs-corrected probe operated at 80 kV.

LEED and ARPES measurements

The ARPES and LEED measurements were carried out at the 4A2 undulator beamline of Pohang Light Source. Air exposure was minimized to a few seconds to avoid surface contamination, and the samples were also annealed at 400 °C for 2 h to remove the contamination layer before the measurement. The ARPES spectra were collected using a Scienta DA30L electron analyser using horizontally linearly polarized photons with an energy of 65 eV. The electrical contact to the ground was made by covering a part of the sample surface with Au foil and the Fermi energies were referred to that of the foil. The photon beam size was 20 × 20 μ m² and the base pressure of the ARPES chamber was maintained below 10⁻¹⁰ torr during the measurements.

SHG measurements

SHG signals were measured under ambient conditions using a femtosecond Ti:sapphire laser with a central wavelength of 800 nm and a pulse

repetition rate of 80 MHz. An objective lens with a numerical aperture of 0.6 was used to focus the laser beam to a spot size of approximately 1 μm and to collect the SHG signals in the backscattering geometry. For spatial mapping of the SHG signals, a piezo-actuated stage was used.

STM sample preparation and analysis

Single-crystal MoS_2 film was loaded into the STM (Omicron) chamber under ultrahigh-vacuum (UHV) conditions (10^{-7} – 10^{-10} torr). Initially, the sample was annealed at 523 K for 10 h to remove the contaminants. Subsequently, Au was deposited at a controlled rate of $\sim 100 \text{ nm s}^{-1}$ under UHV conditions. The sample was then removed and reloaded upside down to detach the MoS_2/Au stack from the sapphire substrate under UHV conditions in the load-lock chamber (base pressure, $<10^{-7}$ torr). STM investigation of the single-crystal MoS_2 ML was performed in the main UHV chamber at 300 K.

Fabrication of MoS_2 Hall-bar device

We used a thermoplastic methacrylate copolymer (Elvacite 2552C, Lucite International) stamp to assemble the hBN/ MoS_2 /hBN stacks in an all-dry manner. The stack assembly process involved heating the stamp to 77 $^\circ\text{C}$ during the pick-up stage and heated to 180 $^\circ\text{C}$ for release. After the stack was successfully transferred, the stamp was dissolved in hot acetone (~ 100 $^\circ\text{C}$) for 1 min. Following this, PMMA was spin coated onto the stack, and it was patterned into a Hall-bar structure using electron-beam lithography and reactive ion etching with a gas mixture of CF_4 and O_2 . To ensure clean MoS_2 edges that are free from contamination, the stacks were treated with in situ Ar^+ sputtering within an electron-beam evaporation chamber. Subsequently, Ti/Au electrodes were deposited via electron-beam evaporation. Once the lift-off process was completed, the Hall devices were subjected to an annealing treatment in an $\text{Ar} + \text{H}_2$ environment at 300 $^\circ\text{C}$ for 3 h to improve the Ti– MoS_2 edge interface, improving the electrical contact quality.

Fabrication of MoS_2 FET arrays

As-grown MoS_2 ML square channels on c-sapphire substrates with patterned SiO_2 trenches were first spin coated with PMMA. These MoS_2 channels were then transferred onto clean HfO_2 (10 nm)/ $\text{p}^+\text{-Si}$ substrates using a water-assisted transfer method. After the transfer, the PMMA layer was removed by soaking the sample in acetone, followed by recoating with a fresh layer of PMMA resist. Electron-beam lithography was used to define the source/drain contact areas, and 10-nm Bi/40-nm Au contacts were deposited via electron-beam evaporation, followed by a lift-off process. To achieve channel isolation, an additional PMMA coating was applied, and electron-beam lithography was conducted to expose and etch away the undesired MoS_2 regions using O_2 plasma, resulting in well-defined MoS_2 channels.

Electron transport measurements

Room-temperature d.c. measurements were performed using a four-probe vacuum station (PS-100) with a base pressure below 10^{-5} torr, connected to a semiconductor parameter analyser (Keithley 4200). For low-temperature electrical measurements, an Oxford Teslatron PT system (TESPT-12-L) was utilized. During Hall measurements, a constant current bias was applied to the channel using a d.c. source (Yokogawa 7651), whereas the gate voltage was controlled by a source measure unit (Yokogawa GS610). Voltage drops across the channel were recorded with voltage amplifiers (ithaco 1201) and digital multimeters (Keithley 2000).

Extraction of phase coherence length from HLN model

The physical parameters describing the weak localization effect can be extracted by using the HLN formula, expressed as

$$\Delta\sigma(B) = \sigma(B) - \sigma(B=0) = \frac{\alpha e^2}{\pi h} \left[\ln\left(\frac{B_\phi}{B}\right) - \Psi\left(\frac{1}{2} + \frac{B_\phi}{B}\right) \right], B_\phi = \frac{h}{8e\tau L_\phi^2},$$

where Ψ represents the digamma function, B_ϕ is the characteristic magnetic field, L_ϕ is the phase coherence length, h is Planck's constant and e is the elementary charge. By fitting the magnetoconductance data in Fig. 4d to the HLN equation (black solid curve), L_ϕ was extracted. This allows for a precise quantification of quantum interference effects in the system.

Data availability

The presented measurement data within this article and the other findings of this study are available from the corresponding author upon reasonable request.

References

- Cui, X. et al. Multi-terminal transport measurements of MoS_2 using a van der Waals heterostructure device platform. *Nat. Nanotechnol.* **10**, 534–540 (2015).
- Fallahazad, B. et al. Shubnikov–de Haas oscillations of high-mobility holes in monolayer and bilayer WSe_2 : Landau level degeneracy effective mass and negative compressibility. *Phys. Rev. Lett.* **116**, 086601 (2016).
- Pisoni, R. et al. Interactions and magnetotransport through spin-valley coupled Landau levels in monolayer MoS_2 . *Phys. Rev. Lett.* **121**, 247701 (2018).
- Rhodes, D., Chae, S. H., Ribeiro-Palau, R. & Hone, J. Disorder in van der Waals heterostructures of 2D materials. *Nat. Mater.* **18**, 541–549 (2019).
- Chen, L. et al. Step-edge-guided nucleation and growth of aligned WSe_2 on sapphire via a layer-over-layer growth mode. *ACS Nano* **9**, 8368–8375 (2015).
- Li, T. et al. Epitaxial growth of wafer-scale molybdenum disulfide semiconductor single crystals on sapphire. *Nat. Nanotechnol.* **16**, 1201–1207 (2021).
- Wang, J. et al. Dual-coupling-guided epitaxial growth of wafer-scale single-crystal WS_2 monolayer on vicinal a-plane sapphire. *Nat. Nanotechnol.* **17**, 33–38 (2022).
- Fu, J.-H. et al. Oriented lateral growth of two-dimensional materials on c-plane sapphire. *Nat. Nanotechnol.* **18**, 1289–1294 (2023).
- Zhu, H. et al. Step engineering for nucleation and domain orientation control in WSe_2 epitaxy on c-plane sapphire. *Nat. Nanotechnol.* **18**, 1295–1302 (2023).
- Zheng, P. et al. Universal epitaxy of non-centrosymmetric two-dimensional single-crystal metal dichalcogenides. *Nat. Commun.* **14**, 592 (2023).
- Li, L. et al. Epitaxy of wafer-scale single-crystal MoS_2 monolayer via buffer layer control. *Nat. Commun.* **15**, 1825 (2024).
- Liu, C. et al. Understanding epitaxial growth of two-dimensional materials and their homostructures. *Nat. Nanotechnol.* **19**, 907–918 (2024).
- Hickey, D. R. et al. Illuminating invisible grain boundaries in coalesced single-orientation WS_2 monolayer films. *Nano Lett.* **21**, 6487–6495 (2021).
- Chubarov, M. et al. Wafer-scale epitaxial growth of unidirectional WS_2 monolayers on sapphire. *ACS Nano* **15**, 2532–2541 (2021).
- Seo, S.-Y. et al. Reconfigurable photo-induced doping of two-dimensional van der Waals semiconductors using different photon energies. *Nat. Electron.* **4**, 38–44 (2021).
- Seo, S.-Y. et al. Writing monolithic integrated circuits on a two-dimensional semiconductor with a scanning light probe. *Nat. Electron.* **1**, 512–517 (2018).
- Seo, S.-Y. et al. Identification of point defects in atomically thin transition-metal dichalcogenide semiconductors as active dopants. *Nano Lett.* **21**, 3341–3354 (2021).
- Ahn, H. et al. Integrated 1D epitaxial mirror twin boundaries for ultrascaled 2D MoS_2 field-effect transistors. *Nat. Nanotech.* **19**, 955–961 (2024).

19. Deng, B. et al. Epitaxially defined Luttinger liquids on MoS₂ bicrystals. *Phys. Rev. Lett.* **134**, 046301 (2025).
20. Jin, G. et al. Atomically thin three-dimensional membranes of van der Waals semiconductors by wafer-scale growth. *Sci. Adv.* **5**, eaaw3180 (2019).
21. Heo, H. et al. Frank–van der Merwe growth versus Volmer–Weber growth in successive stacking of a few-layer Bi₂Te₃/Sb₂Te₃ by van der Waals heteroepitaxy: the critical roles of finite lattice-mismatch with seed substrates. *Adv. Electron. Mater.* **3**, <https://doi.org/10.1002/aelm.201600375> (2017).
22. Jin, G. et al. Heteroepitaxial van der Waals semiconductor superlattices. *Nat. Nanotechnol.* **16**, 1092–1098 (2021).
23. Kyuno, K. & Ehrlich, G. Step-edge barriers on Pt(111): an atomistic view. *Phys. Rev. Lett.* **81**, 5592–5595 (1998).
24. Choi, M.-Y. et al. Thermodynamically driven tilt grain boundaries of monolayer crystals using catalytic liquid alloys. *Nano Lett.* **23**, 4516–4523 (2023).
25. Brewer, L. & Lamoreaux, R. H. The Mo–S system (Molybdenum–Sulfur). *Bull. Alloy Phase Diagr.* **1**, 93–95 (1980).
26. Hoang, A. T. et al. Low-temperature growth of MoS₂ on polymer and thin glass substrates for flexible electronics. *Nat. Nanotechnol.* **18**, 1439–1447 (2023).
27. Fu, D. et al. Molecular beam epitaxy of highly crystalline monolayer molybdenum disulfide on hexagonal boron nitride. *J. Am. Chem. Soc.* **139**, 9392–9400 (2017).
28. Zhang, Z. & Lagally, M. G. Atomistic processes in the early stages of thin-film growth. *Science* **276**, 377–383 (1997).
29. Kim, K. S. et al. Non-epitaxial single-crystal 2D material growth by geometric confinement. *Nature* **614**, 88–94 (2023).
30. Jin, W. et al. Direct measurement of the thickness-dependent electronic band structure of MoS₂ using angle-resolved photoemission spectroscopy. *Phys. Rev. Lett.* **111**, 106801 (2013).
31. Lim, Y.-F. et al. Modification of vapor phase concentrations in MoS₂ growth using a NiO foam barrier ACS nano. *ACS Nano* **12**, 1339–1349 (2018).
32. Zhu, Z. Y., Cheng, Y. C. & Schwingenschlögl, U. Giant spin-orbit-induced spin splitting in two-dimensional transition-metal dichalcogenide semiconductors. *Phys. Rev. B* **84**, 153402 (2011).
33. Jain, A. et al. One-dimensional edge contacts to a monolayer semiconductor. *Nano Lett.* **19**, 6914–6923 (2019).
34. Ma, N. & Jena, D. Charge scattering and mobility in atomically thin semiconductors. *Phys. Rev. X* **4**, 011043 (2014).
35. Datta, S. *Electronic Transport in Mesoscopic Systems* (Cambridge Univ. Press, Cambridge, 1995).
36. Kaasbjerg, K., Thygesen, K. S. & Jacobsen, K. W. Phonon-limited mobility in n-type single-layer MoS₂ from first principles. *Phys. Rev. B* **85**, 115317 (2012).
37. Stern, F. & Howard, W. E. Properties of semiconductor surface inversion layers in the electric quantum limit physical review. *Phys. Rev.* **163**, 816–835 (1967).
38. Ando, T., Fowler, A. B. & Stern, F. Electronic properties of two-dimensional systems. *Rev. Mod. Phys.* **54**, 437–672 (1982).
39. Sarma, S. D., Adam, S., Hwang, E. H. & Rossi, E. Electronic transport in two-dimensional graphene. *Rev. Mod. Phys.* **83**, 407–470 (2011).
40. Schmidt, S. et al. Transport properties of monolayer MoS₂ grown by chemical vapor deposition. *Nano Lett.* **14**, 1909–1913 (2014).
41. Hikami, S., Larkin, A. I. & Nagaoka, Y. Spin-orbit interaction and magnetoresistance in the two dimensional random system. *Prog. Theor. Phys.* **63**, 707–710 (1980).
42. Schmidt, H. et al. Quantum transport and observation of Dyakonov–Perel spin-orbit scattering in monolayer MoS₂. *Phys. Rev. Lett.* **116**, 046803 (2016).
43. Papadopoulos, N., Watanabe, K., Taniguchi, T., van der Zant, H. S. J. & Steele, G. A. Weak localization in boron nitride encapsulated bilayer MoS₂. *Phys. Rev. B* **99**, 115414 (2019).
44. Qu, T. et al. Observation of weak localization in dual-gated bilayer MoS₂. *Phys. Rev. Res.* **6**, 013216 (2024).
45. Shen, P.-C. et al. Ultralow contact resistance between semimetal and monolayer semiconductors. *Nature* **593**, 211–217 (2021).
46. Amani, M. et al. Near-unity photoluminescence quantum yield in MoS₂. *Science* **350**, 1065–1068 (2015).
47. Park, J. H. et al. Defect passivation of transition metal dichalcogenides via a charge transfer van der Waals interface. *Sci. Adv.* **3**, e1701661 (2017).
48. Zhao, Y. et al. Electrical spectroscopy of defect states and their hybridization in monolayer MoS₂. *Nat. Commun.* **14**, 44 (2023).
49. Wang, Y., Sarkar, S., Yan, H. & Chhowalla, M. Critical challenges in the development of electronics based on two-dimensional transition metal dichalcogenides. *Nat. Electron.* **7**, 638–645 (2024).

Acknowledgements

This work was supported by the Institute for Basic Science (IBS), Korea, under Project Code IBS-R034-D1.

Author contributions

G.M., S.-H.L., H. Cho and M.-H.J. conceived and designed the project. S.-H.L., H. Cho, H.P., H.A., J.Y.C., J.-H.K. and C.-J.K. carried out the metal–organic chemical vapour deposition growth experiments and material characterizations. C.-W.C. and S.-Y.C. performed the TEM measurements and analysed the data. G.M., S.-H.S., S.Y.M., S.L. and G.-H.L. fabricated the devices and conducted the electrical measurements. S.Y., Jinjae Kim, H. Choi and Jonghwan Kim performed the optical characterizations, including the PL and SHG measurements. H.J., Jaeyoung Kim and H.W.Y. carried out the LEED and ARPES measurements and analysed the data. J.P. and M.O. acquired the STM images and analysed the data. G.M., S.-H.L., H. Cho and M.-H.J. co-wrote the paper. M.-H.J. supervised the project. All authors discussed the results and provided comments on the paper.

Competing interests

The authors declare no competing interests.

Additional information

Supplementary information The online version contains supplementary material available at <https://doi.org/10.1038/s41928-025-01496-x>.

Correspondence and requests for materials should be addressed to Moon-Ho Jo.

Peer review information *Nature Electronics* thanks Anapum Giri, Vincent Tung and the other, anonymous, reviewer(s) for their contribution to the peer review of this work.

Reprints and permissions information is available at www.nature.com/reprints.

Publisher's note Springer Nature remains neutral with regard to jurisdictional claims in published maps and institutional affiliations.

Open Access This article is licensed under a Creative Commons Attribution-NonCommercial-NoDerivatives 4.0 International License, which permits any non-commercial use, sharing, distribution and reproduction in any medium or format, as long as you give appropriate credit to the original author(s) and the source, provide a link to the

Creative Commons licence, and indicate if you modified the licensed material. You do not have permission under this licence to share adapted material derived from this article or parts of it. The images or other third party material in this article are included in the article's Creative Commons licence, unless indicated otherwise in a credit line to the material. If material is not included in the article's Creative

Commons licence and your intended use is not permitted by statutory regulation or exceeds the permitted use, you will need to obtain permission directly from the copyright holder. To view a copy of this licence, visit <http://creativecommons.org/licenses/by-nc-nd/4.0/>.

© The Author(s) 2025